

The discrepancy between dynamical and stellar masses in massive compact galaxies traces non-homology

Luis Peralta de Arriba^{1,2*}, Marc Balcells^{3,1,2}, Jesús Falcón-Barroso^{1,2} and Ignacio Trujillo^{1,2}

¹*Instituto de Astrofísica de Canarias (IAC), E-38200 La Laguna, Tenerife, Spain*

²*Universidad de La Laguna, Dept. Astrofísica, E-38206 La Laguna, Tenerife, Spain*

³*Isaac Newton Group of Telescopes, E-38700 Santa Cruz de La Palma, La Palma, Spain*

6 December 2019

ABSTRACT

For many massive compact galaxies, dynamical masses ($M_{\text{dyn}} \propto \sigma^2 r_e$) are lower than their stellar masses (M_*). We analyse the unphysical mass discrepancy $M_*/M_{\text{dyn}} > 1$ on a stellar-mass selected sample of early-type galaxies ($M_* \gtrsim 10^{11} M_\odot$) at redshifts $z \sim 0.2$ to $z \sim 1.1$. We build stacked spectra for bins of redshift, size and stellar mass, obtain velocity dispersions, and infer dynamical masses using the virial relation $M_{\text{dyn}} \equiv K \sigma_e^2 r_e / G$ with $K = 5.0$; this assumes homology between our galaxies and nearby massive ellipticals. Our sample is completed using literature data, including individual objects up to $z \sim 2.5$ and a large local reference sample from SDSS. We find that, at all redshifts, the discrepancy between M_* and M_{dyn} grows as galaxies depart from the present-day relation between stellar mass and size: the more compact a galaxy, the larger its M_*/M_{dyn} . Current uncertainties in stellar masses cannot bring M_*/M_{dyn} below 1. Our results suggest that the homology hypothesis contained in the M_{dyn} formula above breaks down for compact galaxies. We provide an approximation to the virial coefficient $K \sim 6.0 [r_e / (3.185 \text{ kpc})]^{-0.81} [M_*/(10^{11} M_\odot)]^{0.45}$, which solves the mass discrepancy problem. A rough approximation to the dynamical mass is given by $M_{\text{dyn}} \sim [\sigma_e / (200 \text{ km s}^{-1})]^{3.6} [r_e / (3 \text{ kpc})]^{0.35} 2.1 \times 10^{11} M_\odot$.

Key words: galaxies: elliptical and lenticular, cD – galaxies: evolution – galaxies: fundamental parameters – galaxies: high-redshift – galaxies: kinematics and dynamics – galaxies: structure.

1 INTRODUCTION

Observations in the last decade have shown that the mean size of massive ($M_* \gtrsim 10^{11} M_\odot$) galaxies evolves with redshift (z), i.e., these galaxies have, at a fixed stellar mass, a smaller size at higher redshifts (e.g. Daddi et al. 2005; Trujillo et al. 2006; Longhetti et al. 2007; Toft et al. 2007; Zirm et al. 2007; Buitrago et al. 2008; Cimatti et al. 2008). The size evolution is more dramatic for early-type galaxies (ETGs) than for late-type galaxies (Trujillo et al. 2007, hereinafter T07). In fact, at $z \sim 2$ a large number of massive ETG galaxies have sizes, as parametrized by the effective radius, of ~ 1 kpc. These objects have been termed massive compact galaxies in the literature. Only few of these galaxies have been found in the nearby Universe (e.g. Trujillo et al. 2009; Taylor et al. 2010; Poggianti et al. 2013; Trujillo et al. 2013).

With the growing availability of velocity dispersion measurements for massive compact galaxies, it has become apparent that dynamical masses, estimated using the virial relation $M_{\text{dyn}} \propto$

$\sigma^2 r_e$, often turn out to be lower than stellar masses. This occurs at low as well as at high redshift. Stockton, Shih & Larson (2010) and Martínez-Manso et al. (2011) found this problem on 2 galaxies at $z \sim 0.5$ and 4 galaxies at $z \sim 1$ respectively. Ferré-Mateu et al. (2012) report the same result for 7 massive compact galaxies in the nearby Universe ($z \sim 0.14$).

As the inequality $M_* > M_{\text{dyn}}$ is unphysical, it follows that, for these objects, either the dynamical masses are underestimated or the stellar masses are overestimated. Both conditions could of course simultaneously apply.

Stellar mass determinations are based on the comparison of galaxy spectral energy distributions (SEDs) with synthetic spectra of stellar populations built using the current knowledge of stellar spectra, stellar evolution, initial mass function (IMF), star formation history and dust attenuation. It is believed that the uncertainty on these parameters can lead to an error in the estimation of the stellar mass up to factors of 2–4 (Conroy, Gunn & White 2009; Muzzin et al. 2009). The comparison with stellar synthesis models can be done using broadband photometric data, hence this

* E-mail: lperalta@iac.es

method provides an efficient means of estimating stellar masses for galaxies at high-redshift.

Several techniques are available to derive dynamical masses. The most accurate methods are based on one of two approaches: the solution of Poisson and Jeans equations (e.g. Satoh 1980), or the description of the system using an orbit-superposition method (Schwarzschild 1979). These methods require high-quality 2-dimensional spectroscopic data, which make them expensive in observing time. A cheaper alternative, and the only one available today for high-redshift galaxies, is to use simpler mass estimators based on the virial theorem. Following the notation in Djorgovski, de Carvalho & Han (1988), we write the virial theorem as:

$$\frac{GM_{\text{dyn}}}{\langle r \rangle} = k_E \frac{\langle v^2 \rangle}{2}, \quad (1)$$

where G is the gravitational constant, $\langle r \rangle$ the gravitational radius of the system, $\langle v^2 \rangle$ is twice the kinetic energy of the system per unit mass, and k_E is the virialization constant. k_E has the value $k_E = 2$ when the system is virialized. Unfortunately, $\langle r \rangle$ and $\langle v^2 \rangle$ are not direct observables. For this reason, it is common to define two coefficients, k_r and k_v , which connect these magnitudes with direct observables that provide galactic length and velocity scales respectively (O_r and O_v). These coefficients are defined by the following equalities:

$$\langle r \rangle = k_r O_r, \quad (2)$$

$$\langle v^2 \rangle = k_v O_v^2. \quad (3)$$

k_r and k_v are respectively coefficients describing the spatial and dynamical structure of the objects. Using equations (2) and (3), it is straightforward to express the virial theorem (equation 1) in terms of observables:

$$M_{\text{dyn}} = K \frac{O_v^2 O_r}{G}, \quad (4)$$

where we have defined K as:

$$K \equiv \frac{k_E}{2} k_v k_r. \quad (5)$$

The coefficient K will be a universal constant only if the coefficients k_r and k_v are the same for all early-type galaxies (or if their dependencies disappear in their product). This hypothesis is known as homology, because it would be verified if all ETGs had the same mass density, kinematic and luminosity structure. Following these ideas, Cappellari et al. (2006) selected the effective (half-light) radius r_e and the luminosity-weighted second moment σ_e of the line-of-sight velocity distribution (LOSVD) within r_e to play the role of observables O_r and O_v , i.e., they used the following equation:

$$M_{\text{dyn}} = K \frac{\sigma_e^2 r_e}{G}. \quad (6)$$

Using a sample of nearby and normal-sized ETGs, these authors found that K is approximately constant and they proposed the next calibration as a reliable estimator of the dynamical mass for an ETG:

$$M_{\text{dyn}} = (5.0 \pm 0.1) \frac{\sigma_e^2 r_e}{G}. \quad (7)$$

This formula has been used in the references mentioned above that lead to the reported discrepancy between dynamical and stellar masses. Hereinafter, we will always use the term dynamical mass to refer to the mass calculated using equation (7).

In this work we have characterized the fraction M_*/M_{dyn} at

different redshifts and covering different regions of the mass-size space. We have used this information to determine in which areas of this parameter space the mass predictions are producing the impossible result $M_* > M_{\text{dyn}}$.

Our paper is structured as follows. In Section 2, we present a description of our sample and additional sources of data. We describe the processing of spectra and velocity dispersion measurements of our sample in Section 3. In Section 4, we show our results for M_*/M_{dyn} and argue that M_* uncertainties alone cannot explain $M_*/M_{\text{dyn}} > 1$ values. We interpret the discrepancy as a non-homology effect in Section 5. In Section 6 we discuss about our results. We summarize our conclusions in Section 7. We adopt a Λ CDM cosmology with $\Omega_m=0.3$, $\Omega_\Lambda=0.7$ and $H_0=70 \text{ km s}^{-1} \text{ Mpc}^{-1}$. The stellar masses are obtained assuming a Salpeter IMF (we have applied a conversion factor when necessary following the prescriptions from Longhetti & Saracco 2009).

2 DESCRIPTION OF THE DATA

2.1 Cross-matching T07 massive galaxies with the DEEP2 DR4 survey

Our targets belong to the catalog of massive galaxies studied by T07. This catalogue contains 796 galaxies with redshifts between 0.2 and 2. These authors split their sample into two groups: one of them contains objects which have a Sérsic index $n < 2.5$ (disc-like galaxies) and another which contains galaxies that verify $n > 2.5$ (spheroid-like galaxies). This criterion is based on the correlation between Sérsic index n and morphological type observed both in the nearby Universe (Ravindranath et al. 2004) as well as in the high- z Universe (see e.g. Buitrago et al. 2013b). In this work, we focus on the spheroid-like galaxies, which are the set with a stronger size evolution. Therefore, our initial catalogue contains the 463 massive galaxies with $n > 2.5$.

An extra requirement we apply to this subsample was the availability of a spectrum in the unique redshift DEEP2 DR4 catalogue (Davis et al. 2003, 2007; Newman et al. 2013). DEEP2 DR4 was designed to conduct a comprehensive census of massive galaxies, their properties, environments, and large-scale structure down to an absolute magnitude $M_B = -20$ at $z \sim 1$. The targets of this catalogue are located in 4 fields, which have a total area of 2.8 deg^2 . One of these fields is the Extended Groth Strip (EGS, Davis et al. 2007). All the galaxies studied by T07 are located in the EGS field. This is relevant because the EGS is the only field of the DEEP2 DR4 survey in which colour pre-selection was not applied.

The cross-match between the DEEP2 DR4 catalogue and the spheroid-like T07 galaxies was done using the *OBJNO* index on the first and the *galaxy identification* on the second. Both indices come from the sample defined by Coil et al. (2004). The number of matches is 260.

Other requirements were applied to this set in order to avoid contaminant objects. Two targets were rejected for being too small to be trustable (they had a semimajor axis equal to 0.01 arcsec and an effective radius $\sim 0.01 \text{ kpc}$). We also required our galaxies to have a secure redshift, i.e., galaxies with quality codes equal to 3 or 4 in the DEEP2 DR4 catalogue. Only in two cases, the difference between the redshift used by T07 (z_{T07}) and the secure redshift published by DEEP2 DR4 (z) was relevant, i.e., they did not verify that $|z_{\text{T07}} - z|/(1+z) < 8$ per cent, $0.89 < z/z_{\text{T07}} < 1.15$ and $|z_{\text{T07}} - z|/z < 13$ per cent. These two targets were rejected. With these extra requirements, our final catalogue was comprises 243 sources.

In Fig. 1 we plot the information of the cross-match between both catalogues in the stellar mass-size diagram. We can see our sample is restricted to $z_{T07} < 1.4$. In the three lower redshift bins most of the points are matches that verify our requirements, but this does not happen in the $z_{T07} \sim 1.25$ bin. A relevant fact that we can check in Fig. 1 is that there are no biases affecting the stellar mass-size distribution in the three lower redshift bins.

2.2 Information taken from T07 and DEEP2 DR4 catalogues

We summarise here the parameters that we will use throughout this work, detailing in each case whether the parameter was extracted from the DEEP2 DR4 or the T07 catalogue, or whether it was derived from a combination of parameters from both catalogues.

- (i) Sérsic index n : taken from the T07 catalogue.
- (ii) Redshift z : taken from the DEEP2 DR4 catalogue, so they are all spectroscopic.
- (iii) Circularized effective radius r_e : effective radii in arcsec were obtained from T07, and afterwards these quantities were converted to kpc using the DEEP2 DR4 redshifts. We compared our effective radii in kpc with T07 radii (r_{eT07}), and checked that they were very similar, i.e., they satisfy that $0.93 < r_e/r_{eT07} < 1.05$.
- (iv) Stellar mass M_* : this magnitude was recalculated based on the T07 stellar masses (M_{*T07}) and considering the DEEP2 DR4 redshift (z) as a small correction of T07 redshift (z_{T07}). Specifically, we considered that an object luminosity should be corrected obeying the equation $L/L_{T07} = [d(z)/d(z_{T07})]^2$, being L the updated luminosity at redshift z , L_{T07} the luminosity at T07 redshift z_{T07} and $d(z)$ is the luminosity distance at a redshift z . We also assumed that the stellar mass-luminosity ratio should be very similar to the considered by T07 for each galaxy, i.e., we used that $M_*/L = k = M_{*T07}/L_{T07}$. These hypotheses imply that the mass correction formula is $M_* = [d(z)/d(z_{T07})]^2 M_{*T07}$. We compared the updated stellar masses with T07 stellar masses and we found that the differences are small ($0.75 < M_*/M_{*T07} < 1.42$).

(v) Individual galaxy spectra: taken from the DEEP2 DR4 survey. These spectra have been obtained using 3 exposures of 20 minutes each with the multi-slit spectrograph DEIMOS (Faber et al. 2003) on the Keck II telescope. The observations were done under seeing conditions between 0.5 and 1.2 arcsec. Their spectral range is 6500–9300 Å and their spectral resolution R is 5900 at 7800 Å. They have a ~ 2 Å gap in the middle of the spectral range, due to the multi-CCD nature of the DEIMOS detector.

2.3 The T07-DEEP2 DR4 sample

Figure 2 shows the mean rest-frame signal-to-noise ratio of the spectra available for each target selected in the Section 2.1 over their stellar mass-size distribution. Most galaxies are located at the three lower redshift bins. As we will use these spectra to make stacked spectra later on and to measure their velocity dispersions, we limit our present sample to targets selected in the Section 2.1 that (i) have spectra with a signal-to-noise ratio greater than 5 \AA^{-1} , and (ii) their redshifts are in the range $0.2 < z < 1.1$.

2.4 Additional data: from SDSS up to high- z galaxies

In Sections 4 and 5 we use additional data in the analysis of our results. We have taken some data of individual galaxies from the literature to explore whether our data is affected by potential

biases due to the stacking process that we have employed in the T07-DEEP2 DR4 sample. All these individual galaxies are massive ($M_* > 10^{11} M_\odot$) and spheroid-like ($n > 2.5$). We have used 6 nearby massive compact galaxies from Ferré-Mateu et al. (2012), 4 galaxies from Stockton et al. (2013) at $z \sim 0.5$ (these galaxies include the 2 galaxies from Stockton, Shih & Larson 2010), and the 4 galaxies from Martinez-Manso et al. (2011) at $z \sim 1$. As we described in the Introduction, for all these galaxies a discrepancy between M_* and M_{dyn} has been reported. We have included dynamical and stellar masses from the compilation of masses and structural parameters for high-redshift individual galaxies done by van de Sande et al. (2013). This compilation has been made using data by van der Wel et al. (2008), Blakeslee et al. (2006), Bezanson et al. (2013), Cappellari et al. (2009), Newman et al. (2010), van de Sande et al. (2013), Onodera et al. (2012), van Dokkum, Kriek & Franx (2009) and Toft et al. (2012), and it covers a redshift range from 0.9 to 2.2. We have also taken 32 massive spheroid-like galaxies from the recent work by Belli, Newman, & Ellis (2013) with redshifts between 1.0 and 1.6.

We also use data from Cenarro & Trujillo (2009), which include results of the Sloan Digital Sky Survey NYU Value Added Galaxy Catalog DR6 (hereinafter SDSS, Blanton et al. 2005; Blanton & Roweis 2007), van der Wel et al. (2005, 2008), di Serego Alighieri et al. (2005) and Cimatti et al. (2008). These authors have provided us with the mean values of individual stellar masses and redshifts. Also, they have given us the mean sizes and velocity dispersions (except for their highest redshift data point, where the mean velocity dispersion is the velocity dispersion on a stacked spectra). In this case we have assigned a mean dynamical mass to each data value introducing the mean values of radius and velocity dispersion in equation (7).

Finally, we have added a sample of 53571 galaxies from the NYU Value-Added Galaxy Catalog DR7. These galaxies were selected using the following criteria: they are massive ($10^{11} M_\odot < M_* < 10^{12} M_\odot$), spheroid-like ($n > 2.5$) and close to the peak of the redshift distribution of the SDSS catalogue ($0.05 < z < 0.11$). To avoid unreliable data, we applied extra restrictions to the SDSS sample: trustable velocity dispersions, physical radii and apparent sizes; i.e., $70 \text{ km s}^{-1} < \sigma < 420 \text{ km s}^{-1}$, $0.3 \text{ kpc} < r_e < 30 \text{ kpc}$, and $r_e > 1 \text{ arcsec}$. The last one is applied to ensure the apparent sizes are larger than the average FWHM ground-based data. Also, we applied the aperture correction for velocity dispersions given in equation 1 of Cappellari et al. (2006), although our results are insensitive to this change.

In Fig. 3 we show the distribution of these additional data on the stellar mass-size diagram.

3 PROCESSING OF SPECTRA AND VELOCITY DISPERSION MEASUREMENTS ON THE T07-DEEP2 DR4 SAMPLE

In order to obtain robust velocity dispersion measurements it is necessary to have a set of spectra with enough signal-to-noise ratio. We reach this goal in our T07-DEEP2 DR4 sample by using the spectral stacking technique. The steps followed by us in the processing of the spectra can be classified in three categories which were applied in the following order: corrections to the individual spectra, stacking of spectra and finally velocity dispersion measurements. The next subsections provide details on each step.

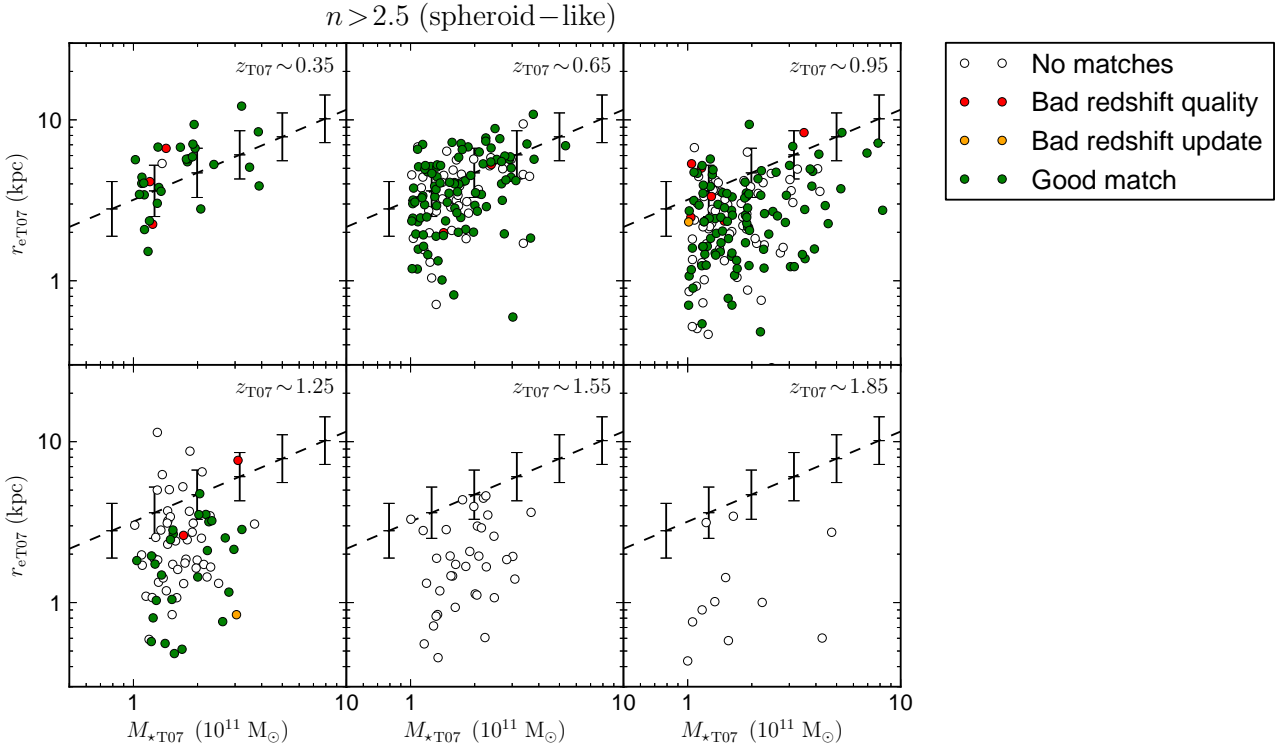


Figure 1. The stellar mass-size distribution of the spheroid-like galaxies ($n > 2.5$) of the T07 sample. In red and orange circles we have plotted the discarded objects because their DEEP2 DR4 redshift is not secure, and the difference between the redshift used by T07 and the secure redshift published by DEEP2 DR4 is relevant (see text for more details). The green circles represent the matches between T07 and DEEP2 DR4 that we have not rejected, while white circles are T07 galaxies without available spectrum in the DEEP2 DR4 sample. The dashed line shows the relation that the ETGs verify in the nearby Universe (Shen et al. 2003). Error bars over-plotted on the dashed line show the dispersion of this relation. Stellar masses, radii and redshifts used in this figure are the same to those used in T07.

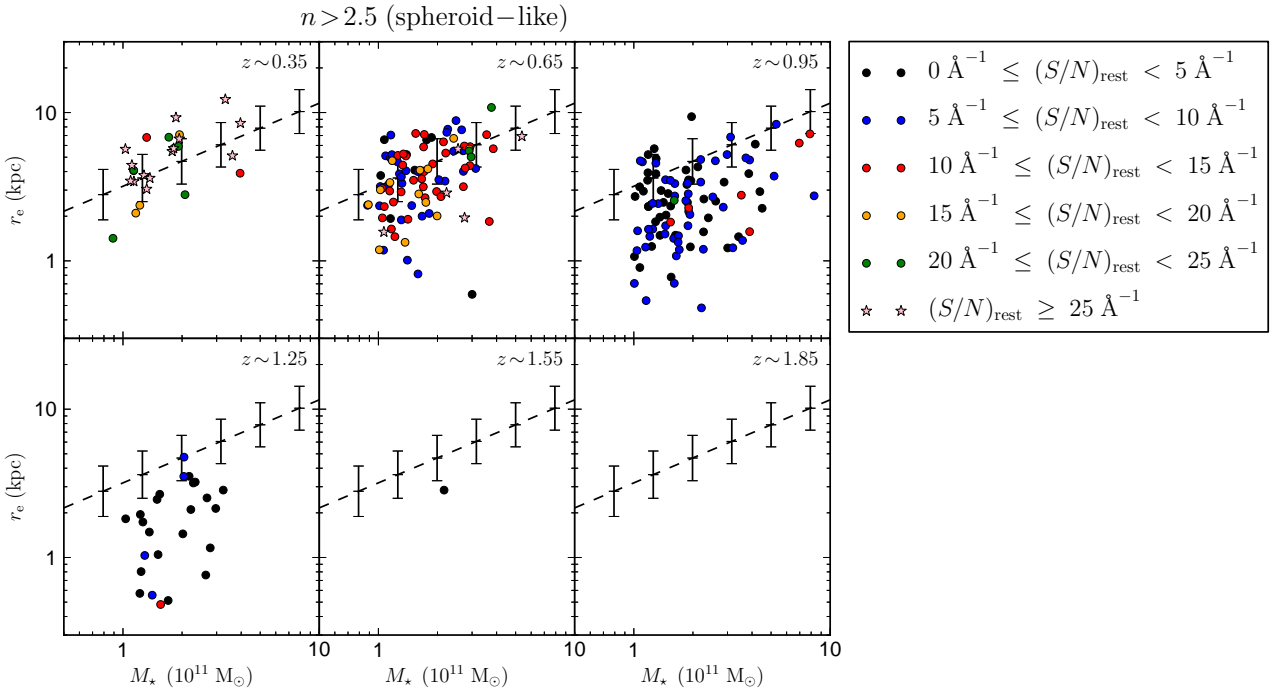


Figure 2. The stellar mass-size distribution of the spheroid-like galaxies ($n > 2.5$) with a good match between T07 and DEEP2 DR4 catalogues. The symbols represent the mean rest-frame signal-to-noise ratio of the DEEP2 DR4 spectra available for each object. The dashed line shows the relation that the ETGs verify in the nearby Universe (Shen et al. 2003). Error bars over-plotted on the dashed line show the dispersion of this relation. Stellar masses, radii and redshifts used in this figure have been determined as explained in Section 2.2.

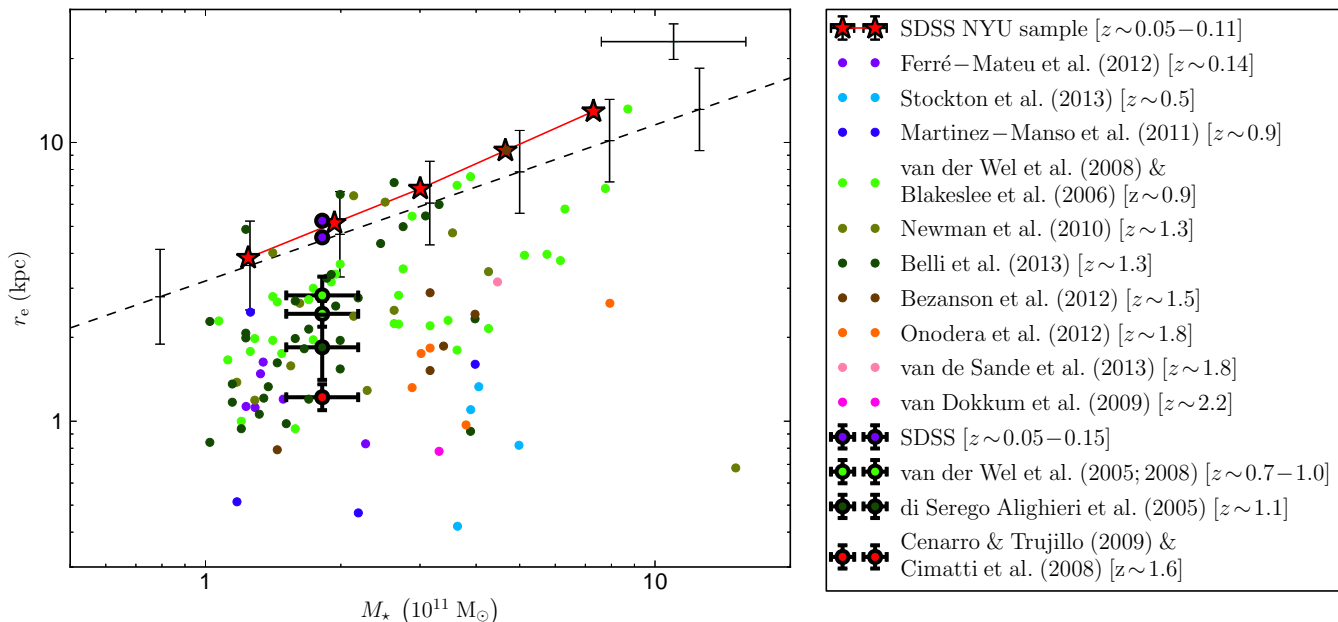


Figure 3. The stellar mass-size distribution of the additional data used in this paper described in Section 2.4. The symbols indicate the origin of each data set. Symbols with/without black edges represent the ‘average’/individual galaxies. For clarity, the SDSS NYU sample has been plotted to show the mean properties of SDSS galaxies after a stellar-mass binning. The dashed line shows the relation that the ETGs verify in the nearby Universe (Shen et al. 2003). Error bars over-plotted on the dashed line show the dispersion of this relation. The error bar cross on the top right corner of the figure represents the mean error of the individual galaxies.

3.1 Corrections to the individual spectra

The corrections applied to the individual spectra were:

(i) *Throughput correction.* The spectra available in the DEEP2 DR4 database are not relative-flux calibrated. To get this calibration, we divide each spectrum by the throughput of the DEIMOS spectrograph (see e.g. Schiavon et al. 2006). We used the data published for an instrumental configuration with the gold 1200 l/mm grating and the OG550 filter¹. For the bluer regions of some spectra, the throughput data are not available, hence we cut that part of the spectra.

(ii) *CCD level relative calibration.* A visual inspection of the spectra shows that about 30 per cent of the spectra have a calibration problem between the 2 CCDs of the spectrograph. We corrected for this by applying a scaling factor to the red region of the spectrum. The scaling factors ranged from 0.6 to 1.5.

(iii) *Pixel masking.* Some spectra have sharp variations at the CCD edges. Also, two telluric absorption bands were identified (they are located at 6860–6922 Å and 7587–7714 Å). These bands belong to the O₂ absorption spectrum (Stevenson 1994). These pixels were masked during the stacking process.

(iv) *Flux normalisation.* We carried out a flux normalisation before the stacking process. For each redshift bin we used a different rest-frame wavelength region: 5500–5700 Å for $0.2 < z < 0.5$, 4500–4700 Å for $0.5 < z < 0.8$, and 4150–4250 Å for $0.8 < z < 1.1$.

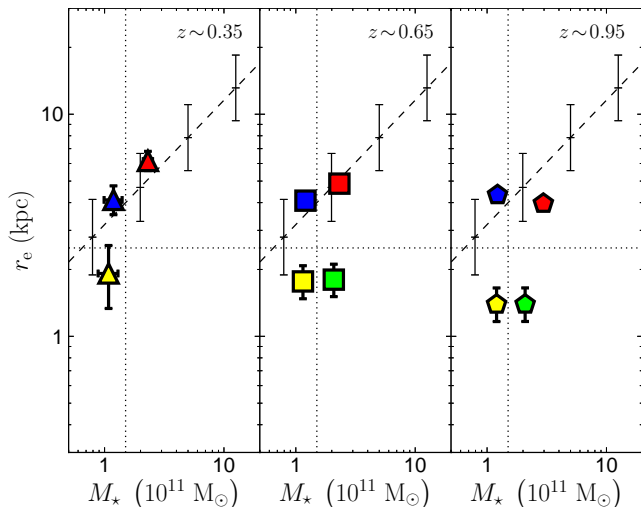


Figure 4. The stellar mass-size distribution of the stacked spectra described in Section 3.2. Symbol shapes indicate different redshift bins, while colours are related to the stellar masses and sizes. Dotted lines show the boundaries used to define each group of stacked spectra. The dashed line shows the relation that the ETGs verify in the nearby Universe (Shen et al. 2003). Error bars over-plotted on the dashed line show the dispersion of this relation.

3.2 Stacking of spectra

We have stacked our spectra in order to reach a signal-to-noise level that let us measure the velocity dispersions with confidence. The stacking process was done as follows:

- (i) Redshift correction to each individual spectrum.
- (ii) Interpolation of each spectrum to a common wavelength vector.

¹ The throughput data for several configurations have been made public in the web-page <http://www.ucolick.org/~ripisc/results.html>.

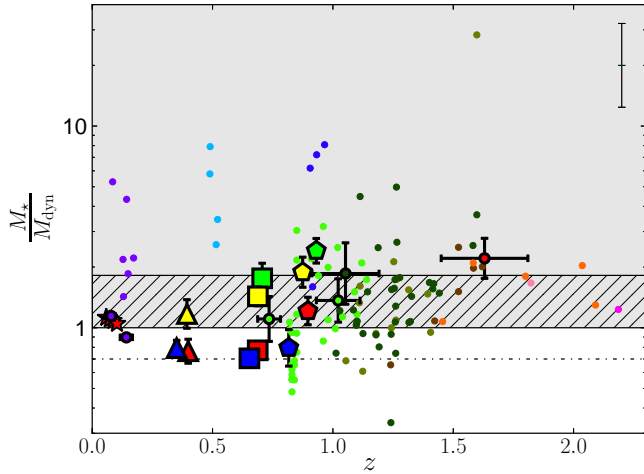


Figure 5. The M_*/M_{dyn} ratio as a function of redshift. The grey region represents the unphysical area where $M_* > M_{\text{dyn}}$. The hatched region covers the sector where the discrepancy between the dynamical and stellar masses could be solved using a Chabrier IMF instead of a Salpeter IMF for the determination of the stellar masses. The dash-dotted line corresponds to a typical stellar/dynamical mass fraction (0.7, see Gavazzi et al. 2007). Symbols are like in Figs 3 and 4. For clarity, the SDSS NYU sample has been plotted to show the mean properties of SDSS galaxies after a redshift binning. The error bar on the top right corner of the figure represents the mean M_*/M_{dyn} error of the individual galaxies. Redshift errors on individual galaxies are smaller than the symbols.

(iii) Mean of interpolated spectra. We used a non-weighted mean, but our essential results remain unchanged if we use a mean where weights are the mean signal-to-noise ratio per \AA of each spectra (these are useful for increasing the signal-to-noise ratio of the stacked spectrum). We have chosen the non-weighted option because signal-to-noise weighting introduces biases towards the brightest galaxies.

We split our sample in three redshift bins ($0.2 < z < 0.5$, $0.5 < z < 0.8$ and $0.8 < z < 1.1$), and each redshift bin was further split in two stellar-mass bins and two effective radius bins. Boundaries were $1.5 \times 10^{11} M_{\odot}$ and 2.5 kpc for mass and size, respectively. A stacked spectrum was built for each bin. Applying this procedure, we got 11 stacked spectra (the high-mass, small-size, low-redshift bin is empty). In Fig. 4 we show the mean stellar masses and radii corresponding to these stacked spectra.

3.3 Velocity dispersion measurements

To compute the velocity dispersion of our stacked spectra, we used the Penalized Pixel-Fitting (pPXF) method by Cappellari & Emsellem (2004). Details of the fitting procedure follow those in Falc3n-Barroso et al. (2011). A relevant pPXF input parameter is the spectral library used to fit each spectrum. We used a set of 82 stars taken from the ELODIE library (Prugniel et al. 2007) that cover a wide range of stellar parameters (T_{eff} , $[\text{Fe}/\text{H}]$, $\log(g)$), which allow us to minimize the impact of template mismatch. Table 1 lists the characteristics of the T07-DEEP2 DR4 stacked spectra, including the results from the velocity dispersion measurements.

To check the robustness of the error velocity dispersion errors, we performed a set of simulations, described in Appendix A. We checked that the error estimations in this simulation are on average 1.8 times higher than the errors of the velocity dispersion

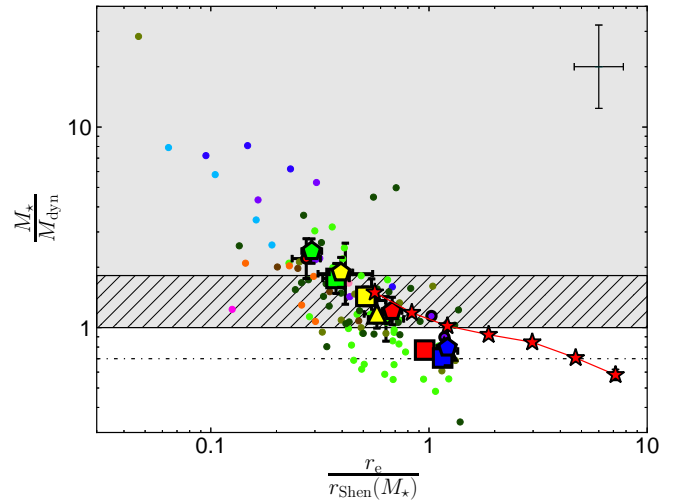


Figure 6. Correlation between the M_*/M_{dyn} ratio and the compactness indicator $r_e/r_{\text{Shen}}(M_*)$. Symbols, regions, dash-dotted line and cross on the top right corner as in Fig. 5. For clarity, the SDSS NYU sample has been plotted to show the mean properties of SDSS galaxies after a binning in $r_e/r_{\text{Shen}}(M_*)$.

measured in the stacked spectra in Table 1, having these ratios a standard deviation of 0.6. As this simulation was developed based on an adverse single stellar population (with 10 Gyr), we conclude that the error estimations in Table 1 represent acceptable values. Furthermore, it is worth noting that although the errors were underestimated by this factor the conclusions of the present paper would be unaltered.

In Appendix B, we have illustrated the pPXF fitting results for the stacked spectra to show the reliability of our spectral fits.

4 DISCREPANCY BETWEEN THE DYNAMICAL AND STELLAR MASSES

We start by comparing the dynamical masses computed using equation (7) with the stellar masses M_* .

Most of the discrepancies between dynamical and stellar masses in the literature have been reported in high-redshift studies. Consequently, an immediate question arises: is this problem related to the redshift of the galaxies? Figure 5 shows that there is not a clear trend between M_*/M_{dyn} and redshift. This figure also shows that there are many galaxies in the forbidden region $M_*/M_{\text{dyn}} > 1$ (grey area in the figure). A conspicuous fact is that our compact galaxies (yellow and green triangles, squares and pentagons) have larger M_*/M_{dyn} than our normal-sized galaxies (blue and red triangles, squares and pentagons). In addition, at low redshift the only conflicting values are the compact massive galaxies from Ferr3-Mateu et al. (2012). Therefore, it is worth asking whether the M_*-M_{dyn} problem is related with the compactness of the galaxies. This would explain why there is a trend to have more galaxies in the grey region at high-redshift in Fig. 5, since it could be connected with the strong size evolution of ETGs with redshift.

To check whether the source of the discrepancy between dynamical and stellar masses is the size of the objects, we need a criterion for measuring the compactness. In this work, we will employ the ratio $r_e/r_{\text{Shen}}(M_*)$, where we have defined the function $r_{\text{Shen}}(M_*)$ as the mean effective (half-light) radius of an ETG in

the nearby Universe. Specifically, $r_{\text{Shen}}(M_*)$ follows the equation:

$$\begin{aligned} r_{\text{Shen}}(M_*) &\equiv 2.88 \times 10^{-6} \text{ kpc} \left(\frac{0.62 M_*}{M_\odot} \right)^{0.56} \\ &= 3.185 \text{ kpc} \left(\frac{M_*}{10^{11} M_\odot} \right)^{0.56}, \end{aligned} \quad (8)$$

where we have considered the fitting result from Shen et al. (2003), and we have introduced the factor 0.62 to adapt the expression from these authors to a Salpeter IMF (Longhetti & Saracco 2009).

In Fig. 6 we plot the fraction M_*/M_{dyn} versus the compactness indicator $r_e/r_{\text{Shen}}(M_*)$. The correlation between the parameters represented in Fig. 6 is strong (Spearman correlation coefficient is -0.75 for all data, and -0.85 for our data). To demonstrate the statistical significance of this correlation we performed two tests. First, we computed the 2-tailed p-value for the Spearman correlation coefficient of all data and our data: 3×10^{-24} and 0.001 respectively. The second test was to calculate the probability of the null result, i.e. whether the distribution of the data is compatible with no relation. To estimate that we calculated the minimum χ^2 value that we can get fitting our data with an horizontal line, and afterwards we computed the probability to get this or higher χ^2 value for the corresponding degrees of freedom. We did this for the individual data and for T07-DEEP2 DR4 data, and the results were 9×10^{-13} and 3×10^{-21} respectively. Also, in this figure we can see that larger M_*/M_{dyn} values are found in most compact galaxies (with several points around a factor of 8 and an extreme data point at ~ 30).

The large ratio between both masses cannot be justified in terms of the weakest aspect of the stellar mass determination: the IMF. Many authors have argued that there is a systematic variation on the IMF in ETGs (Cappellari et al. 2012; Conroy & van Dokkum 2012; Ferreras et al. 2013). However, their results would let us apply a correction factor to each galaxy between 0.5 and 2. This is clearly insufficient to reconcile data with a physically interpretable result. Consequently, one can ask whether the determination of the dynamical mass is the origin of the discrepancy. At this point, we should remember that the determination of M_{dyn} assumes the universality of the coefficient $K = 5.0$ of equation (7). This assumption is based on the homology hypothesis. However, several authors have convincingly argued that ETGs are non-homologous systems (see e.g. Bertin, Ciotti & Del Principe 2002; Cappellari et al. 2006).

We quantify non-homology effects in the next section. Before, and to reinforce our statement, we show in Fig. 7, using a large homogeneous sample of *nearby* galaxies, that the M_*/M_{dyn} ratio increases as the galaxies get compact. Figure 7 shows how the M_*/M_{dyn} ratio varies with the position in the M_* - r_e diagram using the data from the NYU sample of SDSS galaxies. We note that the contours that share the same M_*/M_{dyn} value tend to be parallel to the relation that the ETGs verify in the nearby Universe (Shen et al. 2003) when $r_e/r_{\text{Shen}}(M_*) < 1$. However, above this relation, galaxies with similar M_*/M_{dyn} values seem to depend only on the r_e value and not in the mass.

5 INTERPRETATION OF THE DISCREPANCY AS A NON-HOMOLOGY EFFECT

In this section, we interpret the discrepancy between M_* and M_{dyn} as a non-homology effect, and explain how the discrepancy can be solved using a variation of the K coefficient in equation (6).

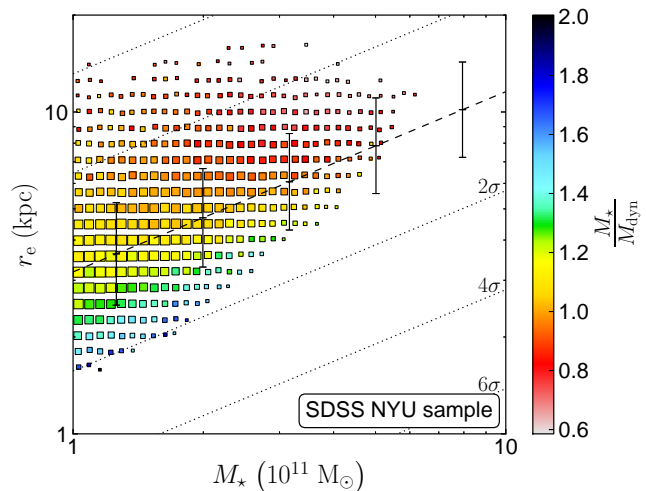


Figure 7. Dependency of the M_*/M_{dyn} ratio with the position in the M_* - r_e diagram for the galaxies in the NYU sample of SDSS galaxies. The data have been binned depending on their stellar masses and radii. The colour of each symbol indicates the M_*/M_{dyn} ratio, while the size of each symbol scales with the number of galaxies of each bin. For clarity, the bins with less than 10 galaxies have been omitted. The dashed line shows the relation that the ETGs verify in the nearby Universe (Shen et al. 2003). Error bars over-plotted on the dashed line show the dispersion of this relation. Dotted lines are parallels to dashed line spaced by 2 times the mean dispersion of the relation from Shen et al. (2003).

Figure 8 shows the dependency of $(M_*/M_{\text{dyn}}) K$ with the compactness indicator $r_e/r_{\text{Shen}}(M_*)$, where the first magnitude was calculated with the formula $(M_*/M_{\text{dyn}}) K = (G M_*)/(\sigma_e^2 r_e)$. Assuming $K = 5.0$, we have drawn two horizontal lines in Fig. 8 for the cases $(M_*/M_{\text{dyn}}) = 0.7$ (Gavazzi et al. 2007) and $(M_*/M_{\text{dyn}}) = 1$ (i.e., no dark matter within the luminous body). We appreciate that there are still many objects above this last line. In fact, it is worth noting that when $r_e/r_{\text{Shen}}(M_*) < 1$, $M_* > M_{\text{dyn}}$ also for galaxies in the SDSS NYU sample if we assume $K = 5.0$. The range of variation of $(M_*/M_{\text{dyn}}) K$ in Fig. 8 is ~ 1.5 dex, while an evolution from a stellar/dynamical mass fraction from 0.7 to 1 only could explain ~ 0.15 dex; in other words, the observed range of $(M_*/M_{\text{dyn}}) K$ is far from being fully explained with the recourse to an increase in (M_*/M_{dyn}) on compact galaxies. The correlation of Fig. 8 has to be dominated by a variation of K . The variations of stellar/dynamical mass fraction of individual galaxies would play the role of a scatter in the relation. This would be true unless there exists a large *systematic* error in the stellar mass determination that scales with compactness. In this section we assume that this is not happening, although we will return to discuss this possibility in our conclusions. Therefore, Fig. 8 indicates a variation in the structure or dynamics of galaxies with compactness, which translates into a K variation.

Can the so-called *weak* homology, where $K = K(n)$, explain the variation of K shown in Fig. 8? Bertin, Ciotti & Del Principe (2002) proposed a variation of K from 8.0 to 1.7 in the Sérsic index n interval [1, 10]; while Cappellari et al. (2006) parametrized this weak homology with K varying from 7.3 to 3.0 when n goes from 2 to 10. Both corrections are much smaller than the required value to explain the range found in Fig. 8. This means that non-homology effects due to compactness are prevailing over weak homology effects.

To characterize the dependency of K with galaxy compact-

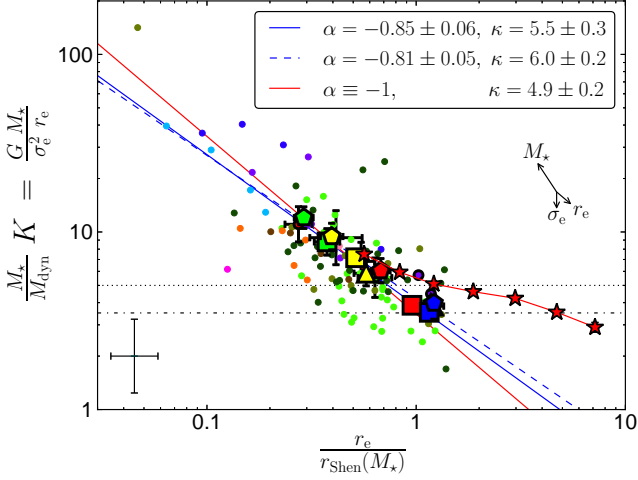


Figure 8. Dependency of $(M_*/M_{\text{dyn}}) K$ with the compactness indicator $r_e/r_{\text{Shen}}(M_*)$. The symbols used in this figure come from Figs. 3 and 4. The dash-dotted black line corresponds to a typical stellar/dynamical mass fraction (0.7, see Gavazzi et al. 2007) and a K value of 5.0 (Cappellari et al. 2006). The dotted black line corresponds to $(M_*/M_{\text{dyn}}) K = 5.0$. Assuming $K = 5.0$, above this line we have the unphysical situation $M_* > M_{\text{dyn}}$. The solid (dashed) blue line is a fit to all (our) data with a law $(M_*/M_{\text{dyn}}) K = 0.7 \kappa (r_e/r_{\text{Shen}}(M_*))^\alpha$. The solid red line is a similar fit to all data where it has been imposed $\alpha \equiv -1$. For clarity, the SDSS NYU sample has been plotted to show the mean properties of SDSS galaxies after a binning in $r_e/r_{\text{Shen}}(M_*)$. The error bar cross on the bottom left corner of the figure represents the mean error of the individual galaxies. The arrows on the right part of the figure indicate that an individual point would have if we would increase its M_* , r_e or σ_e by the mean error on these variables of the individual galaxies.

ness we fit a power law to the data in Fig. 8, i.e.:

$$\begin{aligned} \frac{M_*}{M_{\text{dyn}}} K &= 0.7 \kappa \left(\frac{r_e}{r_{\text{Shen}}(M_*)} \right)^\alpha \\ &= 0.7 \kappa \left(\frac{r_e}{3.185 \text{ kpc}} \right)^\alpha \left(\frac{M_*}{10^{11} M_\odot} \right)^{-0.56\alpha}, \end{aligned} \quad (9)$$

where α and κ are free parameters. α measures the logarithmic slope of K with the compactness; while κ is the value of K for a galaxy which is located in the $z = 0$ stellar mass-size relation with a typical stellar/dynamical mass fraction of 0.7. Making an orthogonal distance regression, all data are fitted with $\alpha = -0.85 \pm 0.06$ and $\kappa = 5.5 \pm 0.3$. Using only our own data gives $\alpha = -0.81 \pm 0.05$ and $\kappa = 6.0 \pm 0.2$. We have plotted these two fits with solid and dashed blue lines in the Fig. 8 respectively. Given that the slope α in our fitting results is similar to -1 , we also determined κ parameter fixing $\alpha \equiv -1$, and we obtained $\kappa = 4.9 \pm 0.2$ (this last fit is plotted in solid red line in Fig. 8). It is remarkable that all κ values are around the $K = 5.0$ value from Cappellari et al. (2006). This result is nevertheless expected because the galaxies employed by those authors in their K calibration were normal-sized ETGs in the $z = 0$ stellar mass-size relation.

Once we have assumed that the variation in Fig. 8 is mainly due to a variation in K , Fig. 9 can be used to understand better our results. This figure shows the K value for each galaxy assuming a fiducial stellar/dynamical mass fraction equal to 0.7 over the stellar mass-size plane. The geometrical meaning of our compactness indicator $r_e/r_{\text{Shen}}(M_*)$ and its relation with K are clear in this figure: when one interprets the M_*-M_{dyn} discrepancy as a non-homology effect, one obtains that two galaxies are homolo-

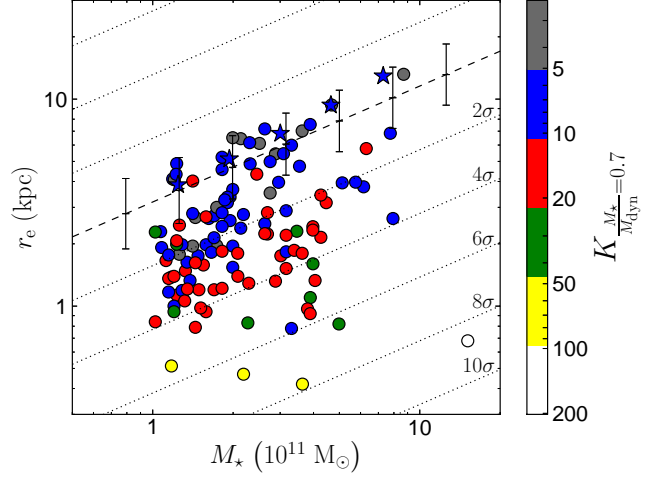


Figure 9. Variation of the K coefficient in the stellar mass-size plane. A typical stellar/dynamical mass fraction in the computation of K ($M_*/M_{\text{dyn}} = 0.7$) has been assumed. The dashed line shows the relation that the ETGs verify in the nearby Universe (Shen et al. 2003). Error bars over-plotted on the dashed line show the dispersion of this relation. Dotted lines are parallels to dashed line spaced by 2 times the mean dispersion of the relation from Shen et al. (2003). For clarity, the SDSS NYU sample has been plotted to show the mean properties of SDSS galaxies after a stellar-mass binning and has been differentiated with star symbols.

gous among themselves, i.e., they have a same K value, if and only if their stellar masses and sizes are in the same parallel line to the relation that ETGs verify in the nearby Universe. In addition, this figure shows the growth of K as a power law of the departure from the $z = 0$ stellar mass-size relation. In that figure we have characterised the departure from the $z = 0$ stellar mass-size relation using the dispersion of this relation (which has the value of 0.154 dex in r_e axis). Also, this figure emphasizes that the galaxies in the $z = 0$ stellar mass-size relation are characterised by sharing the same value of the structural parameter K ($K \sim 5$).

Another way of illustrating the departure from homology (i.e. the variation of K) as a function of the compactness is shown in Fig. 10. Using the NYU sample of SDSS galaxies, we plot the velocity dispersion of the galaxies versus their effective radii. We have split the sample in different stellar mass bins. Figure 10 shows that the galaxies with similar stellar mass do not follow the homology hypothesis (i.e. their σ_e is not proportional to $\sqrt{r_e}$). Interestingly, the departure from the homology is larger when the sizes of galaxies are smaller.

Finally, we provide a *rough* approximation to the K coefficient as a function of the compactness $r_e/r_{\text{Shen}}(M_*)$ using the following expression:

$$\begin{aligned} K &\sim 6.0 \left(\frac{r_e}{r_{\text{Shen}}(M_*)} \right)^{-0.81} \\ &= 6.0 \left(\frac{r_e}{3.185 \text{ kpc}} \right)^{-0.81} \left(\frac{M_*}{10^{11} M_\odot} \right)^{0.45}. \end{aligned} \quad (10)$$

This approximation is based on the fit to our data in Fig. 8, and assumes a fiducial stellar/dynamical mass fraction similar to 0.7 and a Salpeter IMF. We remark that equation (10) should be only used as an estimation within a factor of a few of the K coefficient. If compact massive galaxies are strongly dominated by dark matter, i.e., if they have stellar/dynamical mass fractions lower than ~ 0.3 , equation (10) has to be interpreted as a lower limit to the K coefficient.

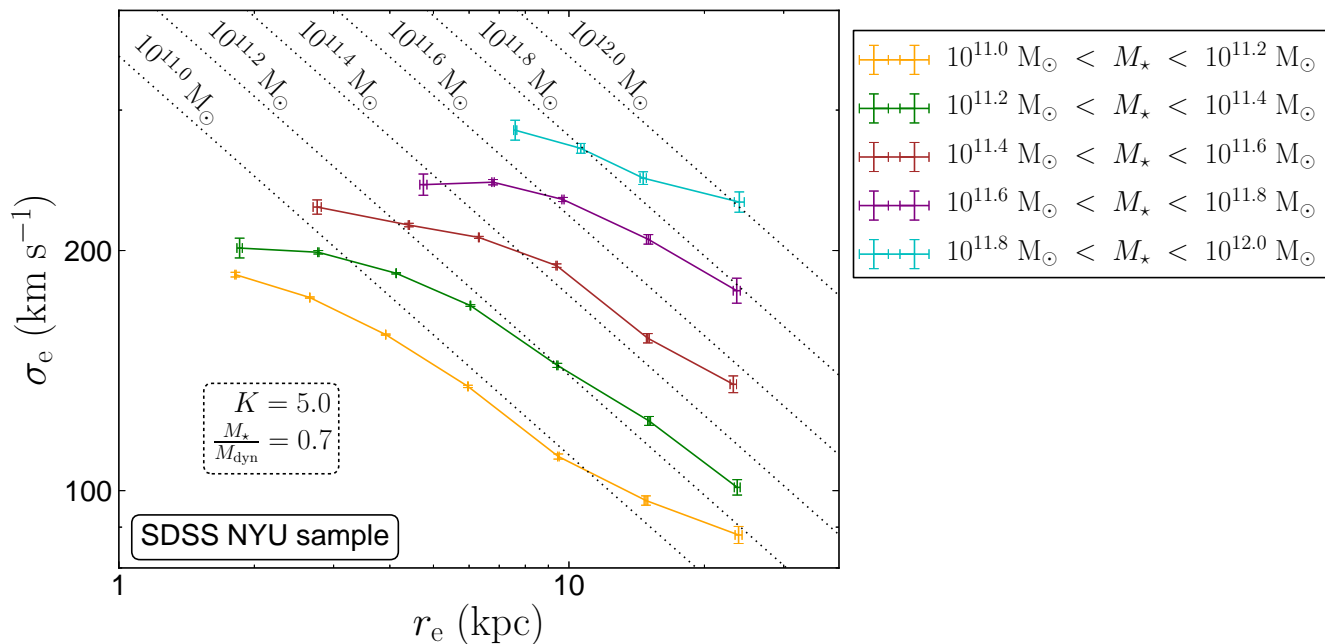


Figure 10. The relation between σ_e and r_e for the SDSS galaxies in the NYU sample. The SDSS NYU data departs from the expectation of the virial theorem when the homology hypothesis is assumed (i.e., $\sigma_e \propto \sqrt{r_e}$). The dotted lines show the prediction for different stellar mass ranges. We have assumed $K = 5.0$ and $M_*/M_{\text{dyn}} = 0.7$ for this prediction.

As a result of the dependency of K with r_e and M_* (equation 10) and using $M_* = 0.7 M_{\text{dyn}}$, the dynamical mass adopts the following dependency on r_e and σ_e :

$$M_{\text{dyn}} \sim \left[7.5 \left(\frac{\sigma_e}{200 \text{ km s}^{-1}} \right)^{1.6} \left(\frac{r_e}{3 \text{ kpc}} \right)^{-0.65} \right] \frac{\sigma_e^2 r_e}{G}$$

$$= \left(\frac{\sigma_e}{200 \text{ km s}^{-1}} \right)^{3.6} \left(\frac{r_e}{3 \text{ kpc}} \right)^{0.35} 2.1 \times 10^{11} M_{\odot}, \quad (11)$$

which highlights that the dependency of M_{dyn} on r_e and σ_e strongly departs from the homology-virial theorem prediction (i.e., $M_{\text{dyn}} \propto \sigma_e^2 r_e$, equation 6 with K independent of σ_e or r_e). We emphasize again that the equation (11) should only be used as an estimate within a factor of a few of the dynamical mass. Of the two factors contributing to the mass discrepancy shown in Fig. 8, equation (11) has corrected the dominant factor, namely compactness, by positing a shallow dependency of M_{dyn} on radius ($\propto r_e^{0.35}$). However, our formula does not address the other factor contributing to mass discrepancy, namely M_*/M_{dyn} , because, by construction, equation (11) gives dynamical masses that fulfil $M_*/M_{\text{dyn}} \sim 0.7$. Still, equation (11) should be useful because the expected departures from $M_*/M_{\text{dyn}} = 0.7$ are small. Therefore, for a galaxy near to $M_*/M_{\text{dyn}} \sim 0.7$, equation (11) estimates approximately the dynamical mass. Conversely, when the baryon density is significantly lower than the dark matter density ($M_*/M_{\text{dyn}} < 0.3$), equation (11) should be considered as a lower limit to the dynamical mass. It is possible to devise corrections to equation (11) if one has independent information on the behaviour of M_*/M_{dyn} .

A question that arises is whether in massive compact galaxies the ratio M_*/M_{dyn} (within $\sim 1 r_e$) significantly departs from the value $M_*/M_{\text{dyn}} = 0.7$ found by Gavazzi et al. (2007). Two-dimensional spectroscopy of compact galaxies, followed by dynamical modelling, will provide the answer to this question. Our guess, in any case, is that, if anything, M_*/M_{dyn} within the lumi-

nous effective radius is higher in an ultra-dense galaxy than in a normal galaxy, given the strongly dissipative processes that must occur in order for the galaxies to reach their high densities. Under this hypothesis, the equation (11) should provide a good approximation to the dynamical mass.

6 DISCUSSION

The family of ETGs may depart from homology (non-constant K in equation 6) through differences in their internal structure, their internal dynamics and/or the contribution of dark matter to their gravitational potential. Structural non-homology is expected given that the surface brightness profiles of ETGs show a range of Sérsic indices n ; Bertin, Ciotti & Del Principe (2002) provide the dependence of K on n . The internal dynamical structure of massive compact galaxies is also expected to differ from that of normal-sized massive galaxies: while the formation of massive compact galaxies must have involved a strongly dissipative collapse, normal-sized $z = 0$ massive ellipticals owe their internal dynamics to a history of dissipationless mergers (see e.g. Trujillo, Ferreras & de La Rosa 2011). Minor mergers, thought to be the dominant mechanism for the size evolution of massive compact galaxies, imply non-violent relaxation which leaves the remnant in a state far from equipartition per unit mass, whereas mixing is more pronounced in major mergers. A further clue that the internal dynamics of massive compact galaxies differs from that of normal-sized ellipticals is provided by the fact that these objects show elongated shapes (Ferré-Mateu et al. 2012; Trujillo et al. 2013), i.e., they have disc-like shapes. At high redshift this is confirmed by van der Wel et al. (2012) and Buitrago et al. (2013b) among others. This fact may suggest an increase of the rotational contribution to dynamical structure of these objects (Buitrago et al. 2013a).

We emphasize that our arguments leading to conclude non-

homology would be compromised if stellar mass estimates were shown to have large, systematic errors that scale with galaxy compactness. The pending task remains to seek clues on non-homology that are independent of stellar mass determinations, using deep two-dimensional spectroscopy of massive compact galaxies to constrain Jeans or Schwarzschild modeling.

7 CONCLUSIONS

On what follows we summarize the main results of this paper.

First, the degree to which the ratio of stellar to dynamical masses is unphysical ($M_*/M_{\text{dyn}} > 1$) is related to the compactness of the galaxies, not to redshift (Figs 5 and 6). For most compact galaxies, the mass discrepancy is too large to be caused by the uncertainties on the IMF, arguably the weakest point in the determination of the total mass of a stellar population. Other uncertainties on the stellar mass determination cannot reconcile both mass estimators either. The disagreement is too large to be explained by a variation in the dark matter fraction. Therefore, either (i) there exists an unknown large *systematic* error in stellar masses linked to galaxy compactness, or (ii) there is a violation of the homology hypothesis in massive compact galaxies.

Second, when we interpret the M_*-M_{dyn} discrepancy in terms of non-homology, i.e., as a variation of the coefficient K from the virial theorem (equation 6), the value of K reaches up to ~ 40 for several compact galaxies (8 times greater than the value found by Cappellari et al. 2006). This strong variation in K is well modelled as $K \propto (r_e/r_{\text{Shen}}(M_*))^\alpha$ with $\alpha \simeq -0.8$.

Finally, due to the dependency of K on r_e and M_* , the dynamical mass scales with σ_e and r_e as $M_{\text{dyn}} \propto \sigma_e^{3.6} r_e^{0.35}$, hence departing from homology and the virial theorem-based scaling $M_{\text{dyn}} \propto \sigma_e^2 r_e$. Equation (11) provides an approximation to estimate M_{dyn} for galaxies with $M_*/M_{\text{dyn}} \sim 0.7$, and is a lower limit for galaxies strongly dominated by dark matter (i.e., $M_*/M_{\text{dyn}} < 0.3$).

ACKNOWLEDGMENTS

We are grateful to the referee for his/her constructive comments that helped to improve the manuscript. The authors thank A. Ferré-Mateu, A. Vazdekis, J. Sánchez Almeida, M. Cappellari, E. Mármol-Queraltó, I. G. de La Rosa, A. de Lorenzo-Cáceres, R. C. E. van den Bosch, F. Shankar, F. Buitrago, A. Stockton and the *Traces of galaxy formation* group (<http://www.iac.es/project/traces>) for their comments during the development of this paper. LPdA is supported by the FPI Program by Spanish Ministry of Science and Innovation. LPdA would like to thank I. Martín-Navarro for fruitful discussions, and V. Alí-Lagoa, L. Toribio San Cipriano and B. González-Merino for comments that helped improve the presentation of our results. JF-B acknowledges the support from the Ramón y Cajal Program from the Spanish Ministry of Science and Innovation, as well as from the FP7 Marie Curie Actions of the European Commission, via the Initial Training Network DAGAL under REA grant agreement number 289313. This work has been supported by the Programa Nacional de Astronomía y Astrofísica of the Spanish Ministry of Science and Innovation under the grants AYA2009-11137 and AYA2010-21322-C03-02. Funding for the DEEP2 Galaxy Redshift Survey has been provided by NSF grants AST-95-09298, AST-0071048, AST-0507428, and AST-0507483 as well as NASA LTSA grant NNG04GC89G. We acknowledge the usage in pPXF of the MPFIT routine by Markwardt (2009).

REFERENCES

- Belli S., Newman A. B., Ellis R. S., 2013, submitted, arXiv:1311.3317
 Bertin G., Ciotti L., Del Principe M., 2002, *A&A*, 386, 149
 Bezanson R., van Dokkum P., van de Sande J., Franx M., Kriek M., 2013, *ApJ*, 764, L8
 Blakeslee J. P., et al., 2006, *ApJ*, 644, 30
 Blanton M. R., Roweis S., 2007, *AJ*, 133, 734
 Blanton M. R., et al., 2005, *AJ*, 129, 2562
 Buitrago F., Trujillo I., Conselice C. J., Bouwens R. J., Dickinson M., Yan H., 2008, *ApJ*, 687, L61
 Buitrago F., Conselice C. J., Epinat B., Bedregal A. G., Grutzbauch R., 2013a, submitted, arXiv:1305.0268
 Buitrago F., Trujillo I., Conselice C. J., Häußler B., 2013b, *MNRAS*, 428, 1460
 Cappellari M., Emsellem E., 2004, *PASP*, 116, 138
 Cappellari M., et al., 2006, *MNRAS*, 366, 1126
 Cappellari M., et al., 2009, *ApJ*, 704, L34
 Cappellari M., et al., 2012, *Nature*, 484, 485
 Cenarro A. J., Trujillo I., 2009, *ApJ*, 696, L43
 Cimatti A., et al., 2008, *A&A*, 482, 21
 Coil A. L., Newman J. A., Kaiser N., Davis M., Ma C.-P., Kocevski D. D., Koo D. C., 2004, *ApJ*, 617, 765
 Conroy C., van Dokkum P. G., 2012, *ApJ*, 760, 71
 Conroy C., Gunn J. E., White M., 2009, *ApJ*, 699, 486
 Daddi E., et al., 2005, *ApJ*, 626, 680
 Davis M., et al., 2003, *SPIE*, 4834, 161
 Davis M., et al., 2007, *ApJ*, 660, L1
 di Serego Alighieri S., et al., 2005, *A&A*, 442, 125
 Djorgovski S., de Carvalho R., Han M.-S., 1988, *ASPC*, 4, 329
 Faber S. M., Jackson R. E., 1976, *ApJ*, 204, 668
 Faber S. M., et al., 2003, *SPIE*, 4841, 1657
 Falcón-Barroso J., et al., 2011, *MNRAS*, 417, 1787
 Ferré-Mateu A., Vazdekis A., Trujillo I., Sánchez-Blázquez P., Ricciardelli E., de la Rosa I. G., 2012, *MNRAS*, 423, 632
 Ferreras I., La Barbera F., de la Rosa I. G., Vazdekis A., de Carvalho R. R., Falcón-Barroso J., Ricciardelli E., 2013, *MNRAS*, 429, L15
 Gavazzi R., Treu T., Rhodes J. D., Koopmans L. V. E., Bolton A. S., Burles S., Massey R. J., Moustakas L. A., 2007, *ApJ*, 667, 176
 Le Borgne D., Rocca-Volmerange B., Prugniel P., Lançon A., Fioc M., Soubiran C., 2004, *A&A*, 425, 881
 Longhetti M., Saracco P., 2009, *MNRAS*, 394, 774
 Longhetti M., et al., 2007, *MNRAS*, 374, 614
 Markwardt C. B., 2009, *ASPC*, 411, 251
 Martínez-Manso J., et al., 2011, *ApJ*, 738, L22
 Muzzin A., Marchesini D., van Dokkum P. G., Labbé I., Kriek M., Franx M., 2009, *ApJ*, 701, 1839
 Newman A. B., Ellis R. S., Treu T., Bundy K., 2010, *ApJ*, 717, L103
 Newman J. A., et al., 2013, *ApJS*, 208, 5
 Onodera M., et al., 2012, *ApJ*, 755, 26
 Pahre M. A., Djorgovski S. G., de Carvalho R. R., 1998, *AJ*, 116, 1591
 Poggianti B. M., et al., 2013, *ApJ*, 762, 77
 Prugniel P., Soubiran C., Koleva M., Le Borgne D., 2007, arXiv, arXiv:astro-ph/0703658
 Ravindranath S., et al., 2004, *ApJ*, 604, L9
 Satoh C., 1980, *PASJ*, 32, 41
 Schiavon R. P., et al., 2006, *ApJ*, 651, L93
 Schwarzschild M., 1979, *ApJ*, 232, 236
 Shen S., Mo H. J., White S. D. M., Blanton M. R., Kauffmann G., Voges W., Brinkmann J., Csabai I., 2003, *MNRAS*, 343, 978
 Stevenson C. C., 1994, *MNRAS*, 267, 904
 Stockton A., Shih H.-Y., Larson K., 2010, *ApJ*, 709, L58
 Stockton A., Shih H.-Y., Larson K., Mann A. W., 2013, *ApJ*, in press, arXiv:1311.5979
 Taylor E. N., Franx M., Glazebrook K., Brinchmann J., van der Wel A., van Dokkum P. G., 2010, *ApJ*, 720, 723
 Toft S., et al., 2007, *ApJ*, 671, 285

Table 1. Characteristics of the T07-DEEP2 DR4 stacked spectra.

ID	$\langle z \rangle$	$\langle M_* \rangle$ ($10^{11} M_\odot$)	$\Delta \langle M_* \rangle$ (dex)	$\langle r_e \rangle$ (kpc)	$\Delta \langle r_e \rangle$ (dex)	$\langle n \rangle$	N_{stack}	$(S/N)_{\text{rest}}$ (\AA^{-1})	σ_e (km s^{-1})	$\Delta \sigma_e$ (km s^{-1})	σ_e^{MC} (km s^{-1})	$\Delta \sigma_e^{\text{MC}}$ (km s^{-1})
(1)	(2)	(3)	(4)	(5)	(6)	(7)	(8)	(9)	(10)	(11)	(12)	(13)
z0.35MR	0.399	2.306	0.04	6.16	0.007	5.8	13	33.9	205	3	204	3
z0.35mR	0.351	1.188	0.012	4.11	0.009	6.0	10	26.6	177	4	180	3
z0.35mr	0.394	1.080	0.03	1.92	0.014	4.4	3	14.9	203	7	201	6
z0.65MR	0.688	2.316	0.02	4.87	0.006	5.5	42	23.9	230	3	230	3
z0.65Mr	0.706	2.080	0.05	1.80	0.010	4.7	7	10.3	238	5	238	6
z0.65mR	0.653	1.204	0.009	4.08	0.011	5.4	21	12.3	190	5	186	5
z0.65mr	0.688	1.147	0.02	1.77	0.015	5.3	16	14.8	177	7	199	6
z0.95MR	0.896	2.960	0.06	3.96	0.015	5.2	21	11.1	230	8	237	7
z0.95Mr	0.931	2.083	0.03	1.39	0.02	4.9	17	10.4	231	9	228	7
z0.95mR	0.817	1.223	0.03	4.33	0.04	4.2	4	5.6	175	17	209	20
z0.95mr	0.874	1.201	0.014	1.39	0.03	5.4	12	8.0	198	11	207	9

Notes to Table 1: (1) Identification associated to the stacked spectra. (2) Arithmetic mean redshift of the individual galaxies used in the stacked spectra. (3) Geometric mean stellar mass of the individual galaxies used in the stacked spectra. (4) Error of the geometric mean stellar mass. (5) Geometric mean effective (half-light) radius of the individual galaxies used in the stacked spectra. (6) Error of the geometric mean effective (half-light) radius. (7) Arithmetic mean Sérsic index of the individual galaxies used in the stacked spectra. (8) Number of stacked individual galaxies. (9) Mean rest-frame signal-to-noise ratio per \AA of the stacked spectra in the region where it was measured the velocity dispersion. (10) Velocity dispersion measured in the stacked spectra. (11) Error of the velocity dispersion measured in the stacked spectra. (12) Mean velocity dispersion measured in 100 Monte Carlo realizations of the stacked spectra. (13) Standard deviation of the velocity dispersion measured in 100 Monte Carlo realizations of the stacked spectra.

Toft S., Gallazzi A., Zirm A., Wold M., Zibetti S., Grillo C., Man A., 2012, *ApJ*, 754, 3
 Trujillo I., Burkert A., Bell E. F., 2004, *ApJ*, 600, L39
 Trujillo I., et al., 2006, *MNRAS*, 373, L36
 Trujillo I., Conselice C. J., Bundy K., Cooper M. C., Eisenhardt P., Ellis R. S., 2007, *MNRAS*, 382, 109 (T07)
 Trujillo I., Cenarro A. J., de Lorenzo-Cáceres A., Vazdekis A., de la Rosa I. G., Cava A., 2009, *ApJ*, 692, L118
 Trujillo I., Ferreras I., de La Rosa I. G., 2011, *MNRAS*, 415, 3903
 Trujillo I., Ferre-Mateu A., Balcells M., Vazdekis A., Sanchez-Blazquez P., 2013, *ApJL*, in press, arXiv:1310.6367
 van de Sande J., et al., 2013, *ApJ*, 771, 85
 van der Wel A., Franx M., van Dokkum P. G., Rix H.-W., Illingworth G. D., Rosati P., 2005, *ApJ*, 631, 145
 van der Wel A., Holden B. P., Zirm A. W., Franx M., Rettura A., Illingworth G. D., Ford H. C., 2008, *ApJ*, 688, 48
 van der Wel A., et al., 2012, *ApJS*, 203, 24
 van Dokkum P. G., Kriek M., Franx M., 2009, *Nature*, 460, 717
 Zirm A. W., et al., 2007, *ApJ*, 656, 66

APPENDIX A: ROBUSTNESS OF THE ERROR DETERMINATION IN THE VELOCITY DISPERSION MEASUREMENTS OF THE STACKED SPECTRA

As an independent check of the accuracy of the velocity dispersion errors delivered by PPF for our T07-DEEP2 DR4 spectra, we have run a set of simulations with synthetic spectra to directly measure errors and their dependency on signal-to-noise ratio and on velocity dispersion.

We first generated a grid of synthetic spectra as follows. We selected a spectrum of a single stellar population of 10 Gyr age and Solar metallicity from the PEGASE library (Le Borgne et al. 2004). We chose this age because it corresponds to a case where it is difficult to measure the velocity dispersion, and the solar metallicity because it represents an average of the expected metallicity. We degraded its spectral resolution to $R = 5900$, the same as the DEEP2 DR4 spectra, and degraded its velocity scale to $13 \text{ km s}^{-1} \text{ pixel}^{-1}$, a mean value of the T07-DEEP2 DR4 spectra at rest-frame. This adapted spectrum was convolved with Gaussian kernels to get 201 broadened versions of the spectrum

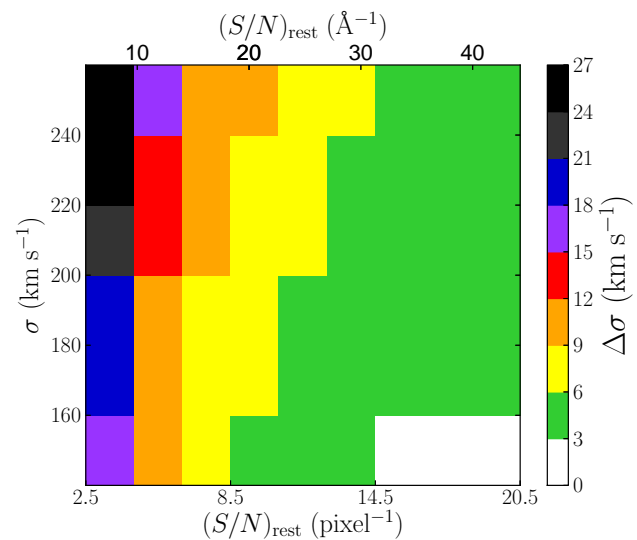


Figure A1. Grid of velocity dispersion deviations from the simulation described in Appendix A as a function of the signal-to-noise and the input velocity dispersion. For clarity, we have binned the data according to their signal-to-noise and σ and computed its standard deviation.

corresponding to velocity dispersions from 140 to 260 km s^{-1} with a step of 0.6 km s^{-1} . With each one of these 201 spectra, we built 61 spectra adding white noise, to obtain spectra with a signal-to-noise from 2.5 to 20.5 pixel^{-1} (separated by 0.3 pixel^{-1}). We finally limited their spectral range from 4100 \AA to 5800 \AA , a representative range of the T07-DEEP2 DR4 spectra at rest-frame. Therefore, we got a grid of 12261 spectra with 201 velocity dispersions and 61 signal-to-noise ratios.

In the next step, we measured the velocity dispersion in each point of the spectral grid, i.e., we ran PPF over 100 Monte Carlo realizations of each spectrum. On the PPF executions, we gave as input parameter the same 82-star spectral library that we used in Sect. 3.3 for fitting the T07-DEEP2 DR4 stacked spectra. We computed the deviation in each point as the difference between the mean value of these measurements and the input velocity dis-

Table A1. Comparison between different ways of estimating the velocity dispersion errors in the T07-DEEP2 DR4 stacked spectra.

ID	$\Delta\sigma_e$ (km s^{-1})	$\Delta\sigma_e^{\text{MC}}$ (km s^{-1})	$\Delta\sigma_{\text{simul}}^{\text{MC}}$ (km s^{-1})
(1)	(2)	(3)	(4)
z0.35MR	3	3	4
z0.35mR	4	3	5
z0.35mr	7	6	9
z0.65MR	3	3	7
z0.65Mr	5	6	17
z0.65mR	5	5	11
z0.65mr	7	6	9
z0.95MR	8	7	16
z0.95Mr	9	7	17
z0.95mR	17	20	25
z0.95mr	11	9	19

Notes to Table A1: (1) Identification associated to the stacked spectra (from Table 1). (2) Error of the velocity dispersion measured in the stacked spectra (from Table 1). (3) Standard deviation of the velocity dispersion measured in 100 Monte Carlo realizations of the stacked spectra (from Table 1). (4) Error of the velocity dispersion obtained from the simulation described in Appendix A.

person (known from the spectral grid generation step). Therefore, we got a grid of velocity dispersion deviations at different velocity dispersions and signal-to-noise ratios. Figure A1 summarizes our results for this grid.

In the last step, we estimated the velocity dispersion errors of each T07-DEEP2 DR4 spectra. We computed these errors as the standard deviation of the grid velocity dispersion deviations inside of a box with size $30 \text{ km s}^{-1} \times 2 \text{ pixel}^{-1}$ around the centre of T07-DEEP2 DR4 spectra properties. In Table A1, we show the comparison between different ways of estimating the velocity dispersion errors in the T07-DEEP2 DR4 stacked spectra, including the results obtained in this last step.

APPENDIX B: FITTING RESULTS FOR THE STACKED SPECTRA

We illustrate in Figs B1, B2 and B3 the pPXF fitting results for the stacked spectra described in Section 3.3 to show the accuracy of the pPXF spectral fitting.

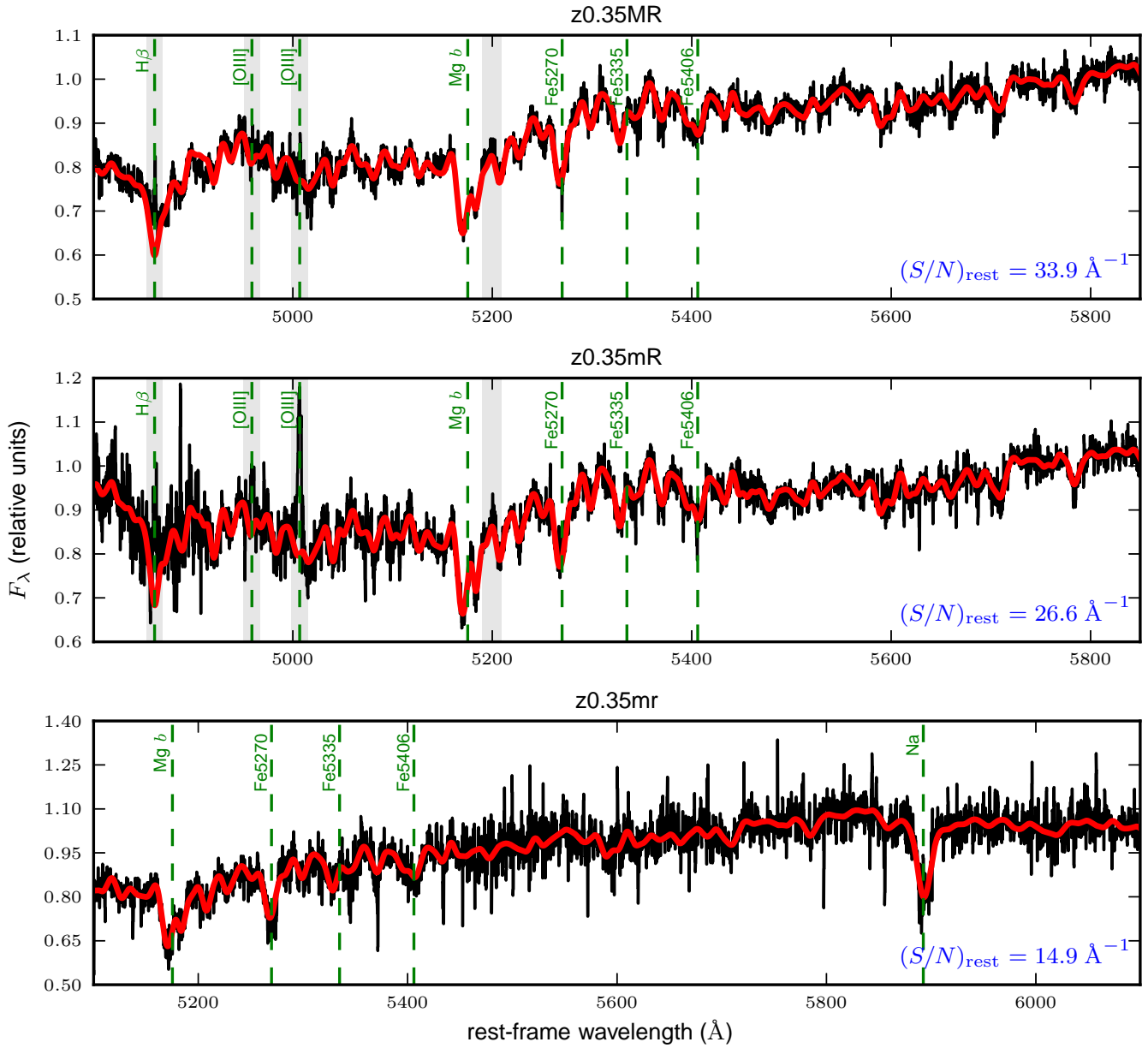


Figure B1. PPXF fitting results for the stacked spectra in the redshift bin $0.2 < z < 0.5$. The black solid lines represent our stacked spectra. Red thick solid lines are the PPXF fits. Masked regions in the PPXF fit are highlighted in grey areas. Some spectral features are marked with green dashed lines to help the reader. Black labels above each panel are the stacked spectrum ID from Table 1. Blue labels on the bottom right corner of each panel indicate the mean rest-frame signal-to-noise ratio per \AA of the stacked spectra in the region where it was measured the velocity dispersion.

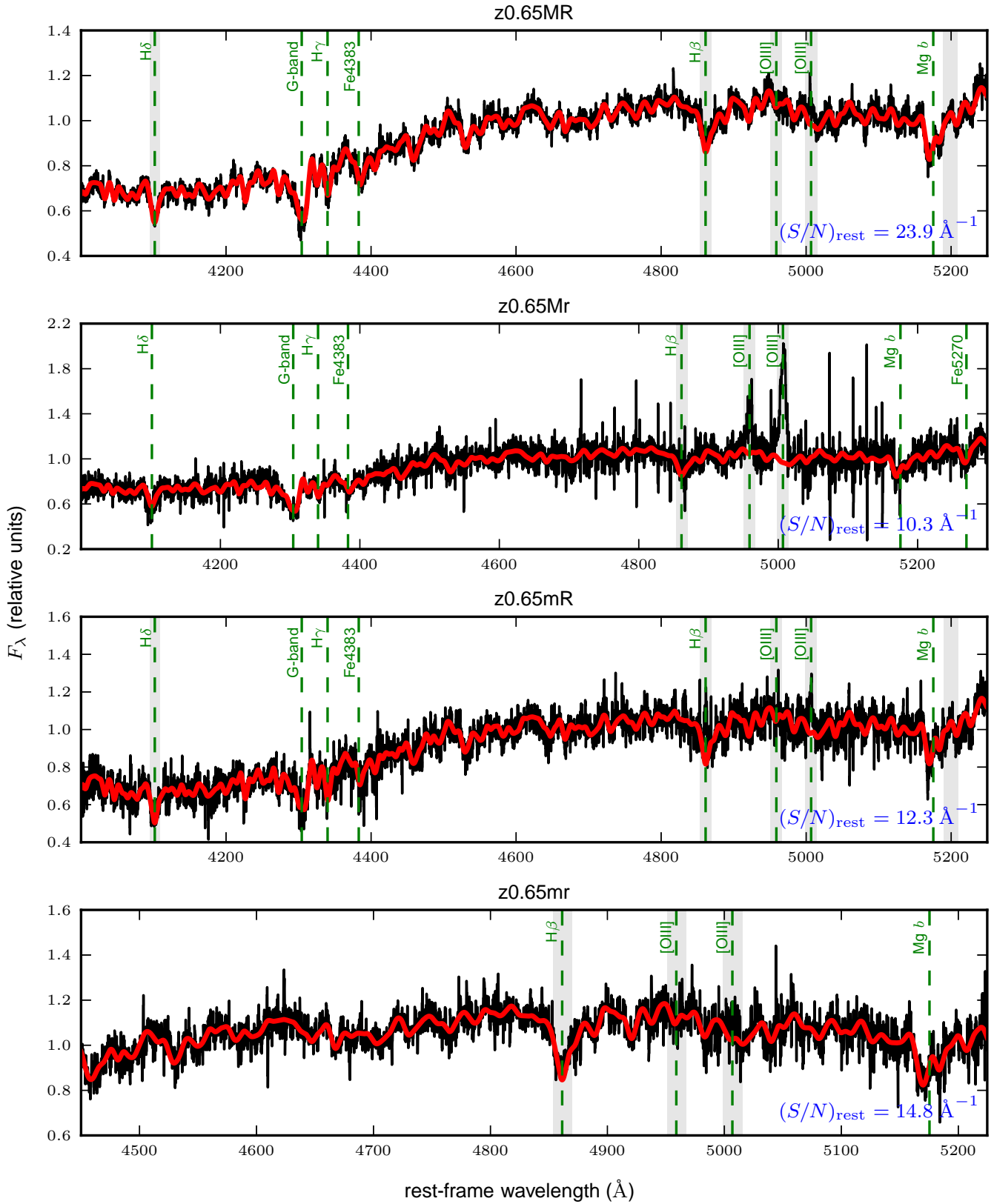


Figure B2. PPXF fitting results for the stacked spectra in the redshift bin $0.5 < z < 0.8$. The black solid lines represent our stacked spectra. Red thick solid lines are the PPXF fits. Masked regions in the PPXF fit are highlighted in grey areas. Some spectral features are marked with green dashed lines to help the reader. Black labels above each panel are the stacked spectrum ID from Table 1. Blue labels on the bottom right corner of each panel indicate the mean rest-frame signal-to-noise ratio per \AA of the stacked spectra in the region where it was measured the velocity dispersion.

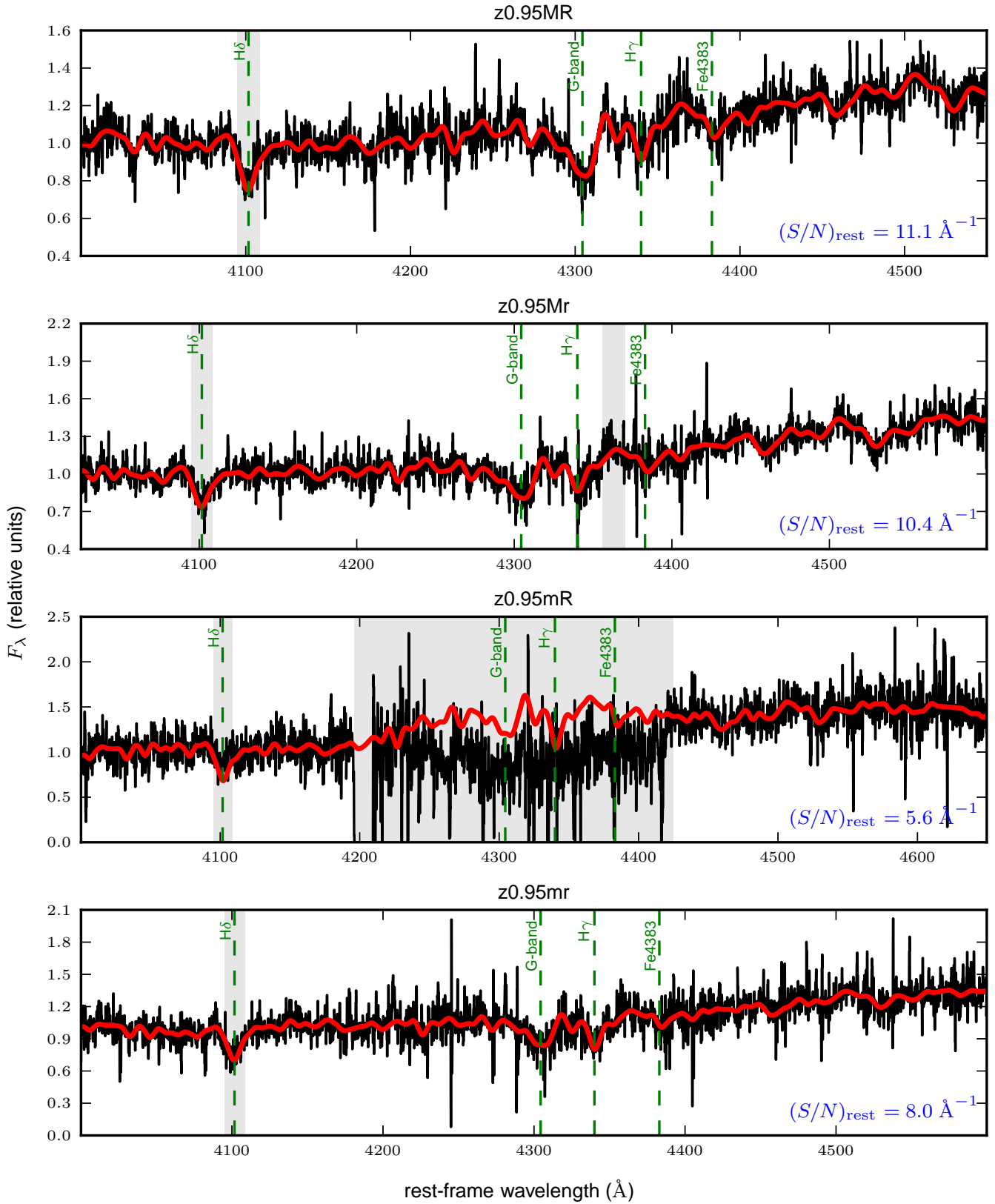


Figure B3. PPXF fitting results for the stacked spectra in the redshift bin $0.8 < z < 1.1$. The black solid lines represent our stacked spectra. Red thick solid lines are the PPXF fits. Masked regions in the PPXF fit are highlighted in grey areas. Some spectral features are marked with green dashed lines. Black labels above each panel are the stacked spectrum ID from Table 1. Blue labels on the bottom right corner of each panel indicate the mean rest-frame signal-to-noise ratio per \AA of the stacked spectra in the region where it was measured the velocity dispersion.